Chapter 1
Super-Resolution Optical Microscopy to Detect Viruses (SARS-CoV-2) in Real Time

C. A. Sciammarella, L. Lamberti, and F. M. Sciammarella

Abstract This article describes the use of evanescent light fields to directly observe and detect the newly discovered coronavirus SARS-CoV-2 that causes COVID-19. The proposed technique provides a low-cost, fast, and highly accurate method of detection. This approach builds from previous work from the authors that enables microscopic observations of nano-objects with the accuracy of nanometers and sensitivities of the order of fraction of a nanometer.

Keywords Optical super-resolution · Evanescent fields · Holography at the nanoscale · Carrier gratings · Digital microscopy · Covid-19 virus · Techniques of detection of covid-19

1.1 Introduction

The observation of objects in the nanometric range is at the cutting edge of current technology and is of paramount importance in the detection of viruses such as the SARS-CoV-2 which causes COVID-19. Currently the virus images are observed with electron microscopes that require freezing the virus at extremely low temperatures. This is a time-consuming and costly process. To effectively combat this virus, it would be critical to make observations of live samples in real time. The authors present previous work that can be extended to the observation of the COVID-19 virus at room temperature using visible light from an optical microscope in real time. In 2009, the authors [1] presented a comprehensive approach using an optical microscope with a methodology that obtained metrological information from prismatic crystals and spheres in the ranges of 10–200 nm that achieved a level of resolution of 0.1 nm, with the accuracy of ±3 nm comparing experimental results with known theoretical sizes.

To achieve the resolution and accuracies with this setup the following conditions must be met. First, it is important to establish an evanescent field within the field of view, via laser light by total internal reflection. The laser light has a similar function to feeding illumination in a laser resonator. It excites the objects to generate light that is defined by the molecular structure of the observed object composition, geometry, and dimensions. The second condition is having the presence of gratings in the optical system. These gratings provide carriers encoding the sought information. The third condition is having a small ball-lens in the sub-millimeter range. This lens acts as a relay in the microscope setup that transmits the near-field information to the far field. At the same time provides the geometry required to produce a nano-resonator in the electromagnetic field. Finally, signal decoding software extracts information from the images that allows reconstruction of the observed objects. Since 2005, the authors made use of evanescent fields in several technical applications [2–7] and in larger fields of view, utilizing several optical configurations. Based on this experience, the authors propose the design of a super-resolution digital microscope that would be capable of observing COVID-19 in real time at an affordable cost. An important characteristic of the system is the utilization of artificial intelligence software to make real-time detection feasible. The following sections will summarize the main topics necessary to set the foundations of the proposed technology.

C. A. Sciammarella (✉)
Department of Mechanical, Materials and Aerospace Engineering, Illinois Institute of Technology, Chicago, IL, USA
e-mail: sciammarella@iit.edu

L. Lamberti
Dipartimento Meccanica, Matematica e Management, Politecnico di Bari, Bari, Italy

F. M. Sciammarella
MxD, Chicago, IL, USA

S. L. B. Kramer et al. (eds.), *Thermomechanics & Infrared Imaging, Inverse Problem Methodologies, Mechanics of Additive & Advanced Manufactured Materials, and Advancements in Optical Methods & Digital Image Correlation, Volume 4*, Conference Proceedings of the Society for Experimental Mechanics Series, https://doi.org/10.1007/978-3-030-86745-4_1

1.2 Background on the Generation of Optical Signals at the Near Field

When analyzing super-resolution images to obtain both shape and size, it is necessary to understand the processes of generation of the signals that contain information about the properties and dimensions of the objects. There are two basic ranges that depend on the relationship of the illuminating beam wavelength λ to the dimensions of the observed objects. The dimensions of the object are such that minimum dimension dmin> λ, and the other case is when the dimensions of the object are smaller than the wavelength of the object, dmin<λ. In the case of objects smaller than the wavelength of light let us consider a simple case, observations of prismatic shapes. Experimental evidence shows that observing a face of a prism, for example, the face with dimensions [Lo, Wo], Fig. 1.1, one gets 3 shifted images (Fig. 1.2) corresponding to three partially overlapping wavefronts. In [1] a model was introduced for the signal generation by objects smaller than the wavelength of light, nanocrystals, nanospheres. The model is based in the Brillouin scattering process in the ultrasound range [8, 9]. Scattering in this context means collision between particles, in this case collision between phonons and electrons. The Brillouin scattering in the ultrasound range is based in the piezo-electric effect in materials. Piezoelectric effect is the ability of certain materials to generate electric charges in response to applied mechanical stresses. An acoustic wave is generated in a crystal that propagates with the velocity of sound in the material medium. This acoustic wave produces the conversion of mechanical energy of the deformed into the electro-magnetic energy of emitted light.

The process of getting the crystal dimensions gives an insight on the different steps that lead to the determination of the prism proportions. Dimensional information is obtained through the eigen mode of vibration of the prism. The prism vibrates axially along the symmetry axis, alternatively expanding and contracting. The phenomenon that produces the observed shifted images of a wavefront is called Bragg's diffraction, in analogy to X-ray diffraction where a similar process takes place. The acousto-optic effect is akin to the photoelastic effect, in the sense that the permittivity ε of an observed crystal is changed due to strain components ε_{ij}. The equivalent of a standing diffraction grating is formed by the sound waves propagating in the medium. Through this process mechanical energy is transmitted to the electronic field. This diffraction pattern is characterized by a diffraction angle θ_n with respect to the direction of propagation of the light wavefront, and is given by,

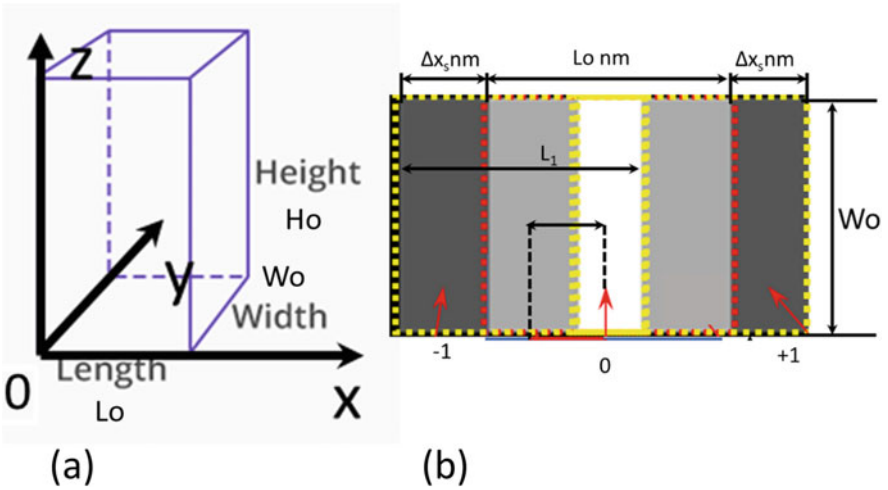

Fig. 1.1 (**a**) Rectangular prismatic single crystal; (**b**) Observed face Lo X Wo of a prism, three shifted images of the face are observed

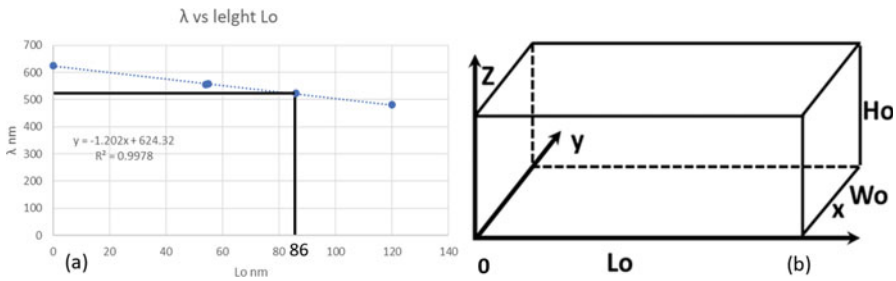

Fig. 1.2 (**a**) Wavelength λ of the resonant modes as a function of the crystals length Lo; (**b**) Observed single crystals geometry and corresponding reference axis

$$\sin\theta_n = n\frac{\lambda}{2\Lambda} \tag{1.1}$$

In Eq. (1.1) λ is the wavelength of the optical wave, Λ is the wavelength of the acoustic wave and n is the diffraction order of the generated light. Due to energy considerations most of the energy concentrates in two diffraction orders. The resonance modes in the electromagnetic field of the observed crystals produce the emission of wavelengths that depend on two fundamental factors, the chemical composition of the crystal and on the dimensions of the crystal. This model predicts that the wavelength of light generated by a given crystal is a function of the length of the crystal Lo. The Lo designation is given taking into consideration the position of the prism with respect to the illuminating laser beam and the excited eigen mode in the prism. This prediction is confirmed by the graph of Fig. 1.2 where experimental data of the wavelengths determined for different nanocrystals of sodium chloride are plotted together with the values predicted by the model of [1].

Figure 1.3 is an additional experimental proof that the light emitted by a crystal as predicted by the developed model is a function of the crystal length. Figure 1.3a is a gray scale image of one of the observed crystals, Lo = 86 nm. Figure 1.3b is a color image of the same crystal. Although the geometrical scales of both images are not the same, visually it is possible to see that both images correspond to the same crystal. As mentioned before, the illuminating laser wavelength is $\lambda = 0.6328$ μm, the wavelength of the observed image is, Fig. 1.4, 524 nm that corresponds to a light green hue. Figure 1.4 shows that it is possible to get the prism dimensions Lo and Wo from the images captured within the setup. The other unknown dimension of an observed prism is Ho, the height of the prism.

Figure 1.4a shows the enlarged image of a nanocrystal. Figure 1.4b shows the atomic reconstruction of the crystal from theoretical considerations based on monomers of the crystal, also showing the corresponding reference Cartesian-axes. Figure 1.4c shows the sizes Lo and Wo of the crystal obtained by utilizing edge detection algorithms and shows the amount of the image shift. Two of the 3 unknows are determines as it is shown in this example. It is now necessary to obtain the magnitude of Ho, the third unknown, the depth of the nanocrystal. There are two techniques that are possible to apply [1]. One is based on the magnitude of the shift Δx_s, Fig. 1.3c. We will explain the second technique that is based on the principles of the observation of phase objects in holographic interferometry.

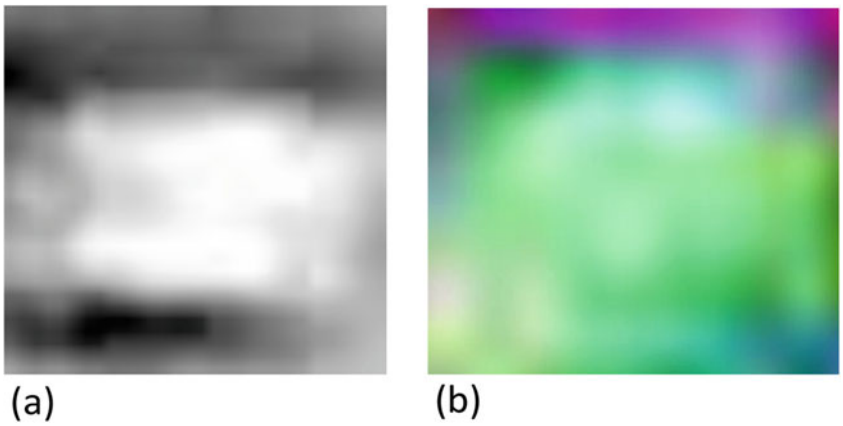

Fig. 1.3 NaCl nanocrystal of length 86 nm: (**a**) grayscale image; (**b**) image of the crystal captured by a color camera

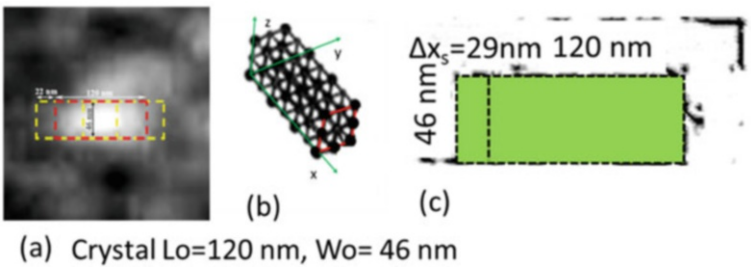

Fig. 1.4 (**a**) Enlargement of area surrounding the crystal; (**b**) Atomic model of the nano-monomer of the sodium chloride; (**c**) contour of the crystal and of the shifted image obtained using edge detection

In the second technique, technique, we make use of the different diffraction orders of a grating and it is a major component of the optical setup utilized to obtain the images of the nanocrystals. Let us consider the quasi-monochromatic coherent scalar wave emitted by a nano-sized crystal. The actual formation of the image of the nanocrystal is similar to a typical lens hologram of a transparent object illuminated by a grating. The gratings are carrier gratings that can be utilized to extract optical path changes. This type of setup to observe phase objects has been used in phase hologram interferometry as a variant of the original setups [10, 11]. When the index of refraction in the medium is constant, the rays going through the object are straight lines. The prismatic object emits a beam normal to its faces; the optical path s_{op} through the prism is given by the integral,

$$s_{op}(x,y) = \int_0^t n_i(x,y,)\,dz \tag{1.2}$$

In Eq. (1.2) the direction of propagation of the beam is the z-coordinate and the analyzed plane wavefront is the plane x–y; $n_i(x,y,z)$ is the index of refraction of the medium.

The change experienced by the optical path is given by,

$$\delta_{op}(x,y) = \int_0^t \left[n_i(x,y,z) - n_o\right]dz \tag{1.3}$$

In Eq. (1.3) t is the thickness of the medium (called Ho in Fig. 1.1). Assuming that:

$$\mathrm{n_i(x,y,z) = n_c} \tag{1.4}$$

In Eq. (1.4) n_c is the index of refraction of the observed nanocrystals, Eq. (1.4) then becomes,

$$\delta_{op}(x,y) = \int_0^t \left[n_c(x,y,z) - n_o\right]dz = (n_c - n_o)t \tag{1.5}$$

By transforming Eq. (1.5) into phase differences and making $n_o = n_s$, where n_s is the index of refraction of the saline solution containing the nanocrystals, one can write:

$$\Delta\Phi = \frac{2\pi}{p}(n_c - n_s)t \tag{1.6}$$

In (1.6) p is the pitch of carrier grating whose phase has experienced the change $\Delta\phi$ going through the thickness of the nanocrystal Ho, Fig. 1.1. The carrier pitch is modulated by the thickness of the nanocrystal. For a given diffraction order the optical path is a linear function of the thickness, the evanescent diffraction order 0 is normal of the surface of the nanocrystals. The conclusion is then that the same treatment utilized in classical holographic interferometry of transparent objects can be utilized for the nanocrystals depth measurement. For each analyzed crystal, a particular pitch p of the carrier is selected from the FT of the image. The frequency of interest is individualized in the background of the observed object and a diffraction order is selected and filtered. In a second step, the selected order is located in the FT of the observed object. A filter size is then adopted to pass additional of harmonics that correspond to the modulation of the carrier produced by the thickness Ho. Those additional frequencies carry the information of the change in phase produced by the change of optical path. In the next step, the phase of the modulated carrier and the phase of the unmodulated carrier are computed. The change of phase is introduced in Eq. (1.6) and the value of Ho is computed. The phase difference may not be constant throughout the prismatic crystal face

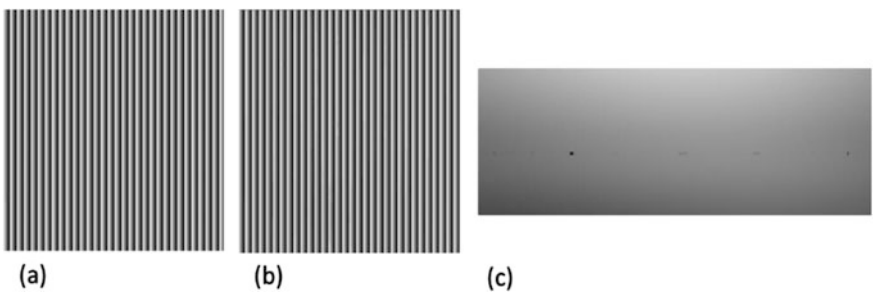

Fig. 1.5 Phase determination for the nanocrystal of length L = 120 nm: (**a**) reference phase of the carrier fringes; (**b**) phase of carrier fringes modulated by the nanocrystal; (**c**) phase difference in the region of the nanocrystal represented in levels of gray

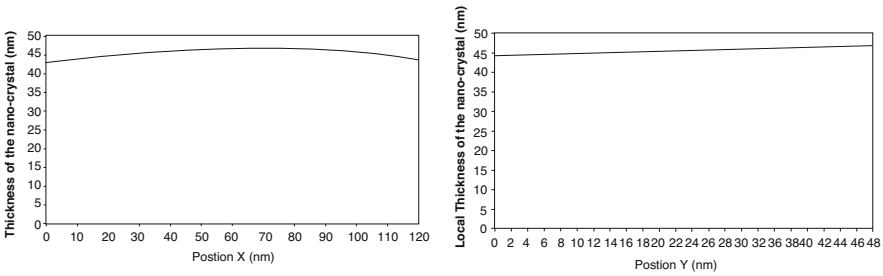

Fig. 1.6 (**a**) Cross section of the crystal Lo = 120 nm along the x-axis; (**b**) Cross section of the crystal Lo = 120 nm along the y-axis

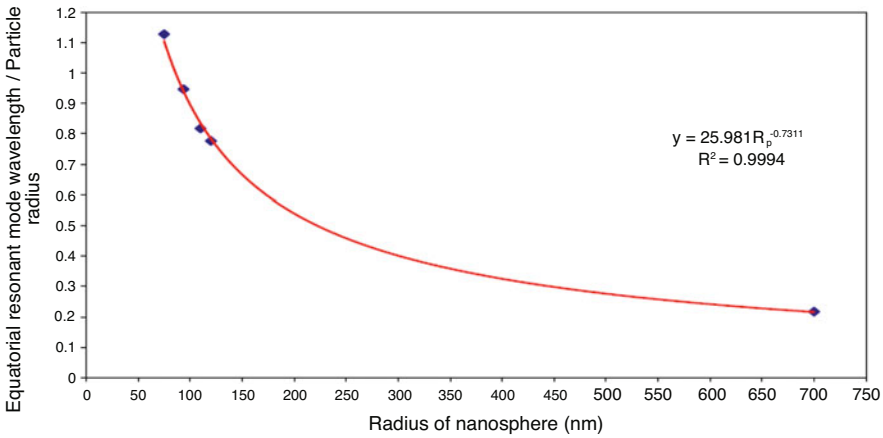

Fig. 1.7 Correlation of the nanospheres radius and the equatorial wavelength expressed as a fraction of the radius

since it is unlikely that the crystal face is parallel to the image plane of camera. Therefore, an average thickness is computed. Hence, depth can be computed as an average of the depth coordinates of points of the face. Figure 1.5 illustrates, for the crystal of Lo = 120 nm, the different steps of the process described above. The reference phase pattern corresponds to a carrier in a region near but not in the correspondence with the crystal image. It is acquired by applying in the FT of the image a 1×1 filter (Fig. 1.5a) corresponding to the pitch p = 5.53 nm. The carrier modulated by the thickness of the crystal, Fig. 1.6b, is obtained by selecting the FT of the image of the same order selected in the background but with a filter that allows additional orders to pass. Figure 1.5c represents the change of phase in gray levels. Figure 1.6a represents the cross section of the crystal along the longitudinal direction, coordinate x. Figure 1.6b represents a transversal cross section in the y-direction. The value of the depth resulting from averaging the phase plotted in Fig. 1.5c is 46 nm.

1.3 Observation of Nanospheres

The same principle that applies to the formation of images that was presented in Sect. 1.2 for nano prismatic crystals is valid also in the case of nanospheres; the observed pattern of resonance is a function of the length of the perimeter of the equatorial circle of the excited form of vibration of the nanosphere. Micro/nanospheres made of transparent dielectric media are excellent optical resonators. Both theoretical and experimental studies on the resonant modes of micro/nanospheres are available in the literature. Of particular interest are the modes localized on the surface of the sphere, along the equator. These modes are called *whispering gallery modes* (WGM). WGM result from light confinement due to total internal reflection inside a high index spherical surface immersed in a lower index medium. Of all resonant geometries a sphere has the capability of storing and confining energy in a small volume. Figure 1.7 shows the correlation between the nanospheres radius and the equatorial wavelength expressed as a fraction of the corresponding radius. It is interesting to point out that the point corresponding to $r = 700$ nm corresponds to a numerical solution of a polystyrene nanosphere [12]. There is an excellent agreement between the experimental values the authors obtained and the numerical solution, $R^2 = 0.9994$.

1.3.1 Optical Setup

The optical system consists of a CCD camera attached to a digital microscope. Figure 1.8 represents the optical arrangement. A glass sphere is supported on a microscope slide; this sphere has a dual role. The sphere acts as a ball lens in the microscopic system, at the same time as it will explained later, contributes to the generation of the electromagnetic field that produces the images of the nano-objects. The optimal numerical aperture of the object space of the spherical lens is limited by the spherical aberrations. The spherical aberration limits the maximum achievable resolution in the image. The optimal theoretical position of the ball lens pupil is in the center of the ball lens. Since such a configuration is difficult to implement, the next practically acceptable position for the aperture stop is directly behind the ball lens, in this case the surface of the supporting glass slide. The focal distance f of this lens can be computed using the equations of geometric optics. The source of the illumination generating the image of the nanospheres and the carrier gratings covering the image of the nanospheres as we have seen are the resonant electro-magnetic oscillations generated in the observed objects by the laser beam. The whole region of contact between the observed objects and the microscope slide is the equivalent of a micro-laser resonator. The light is generated in the nano-objects and focused on the focal plane of the microlens. The digital microscope shown in Fig. 1.8 is focused to the plane of best contrast of the image, which is close to the ball lens focal plane. The image is not formed by plane wave fronts illuminating the nano-objects, as is the case with the classical Mie's solution for a diffracting objects. In the present case, a large number of evanescent waves impinge in the nano-objects and then generate propagating wave fronts. The wavefronts emitted by the nano-objects have the structure of pseudo non-diffracting propagating waves. The light emission by the nanospheres is produced by multi-polar resonance of the nano-objects caused by the electromagnetic field generated by the evanescent waves. Evanescent beams are converted into actually propagating beams when they interact with the nano-objects. A complete analysis requires a vectorial solution of the Maxwell equations; as a first approach a scalar form can be utilized. The observed light fields can be considered as solutions of the Helmholtz equation.

$$\left(\nabla^2 + k^2(r)\right) W(r,\theta) = 0 \tag{1.7}$$

In Eq. (1.7) (r,θ) denotes the transverse coordinates, ∇^2 is the Laplacian, $k(r)$ is the wave vector, $W(r,\theta)$ is the scalar electromagnetic field. These waves produce images in the camera attached to the microscope. The pseudo non-diffracting wavefronts can travel long distances or go through an optical system without the diffraction changes experienced by ordinary wavefronts. The validity of this approach is supported in the following references [13–16].

Figure 1.8 shows a detailed view that graphically illustrates the process of formation of gratings that produce the lens-holograms of the observed nanospheres. The gratings are the interaction of the nano-object with the evanescent field. The application of the microscope that is depicted in Fig. 1.8 is the examination of human saliva in a saline solution contained in a depression well standard slide.

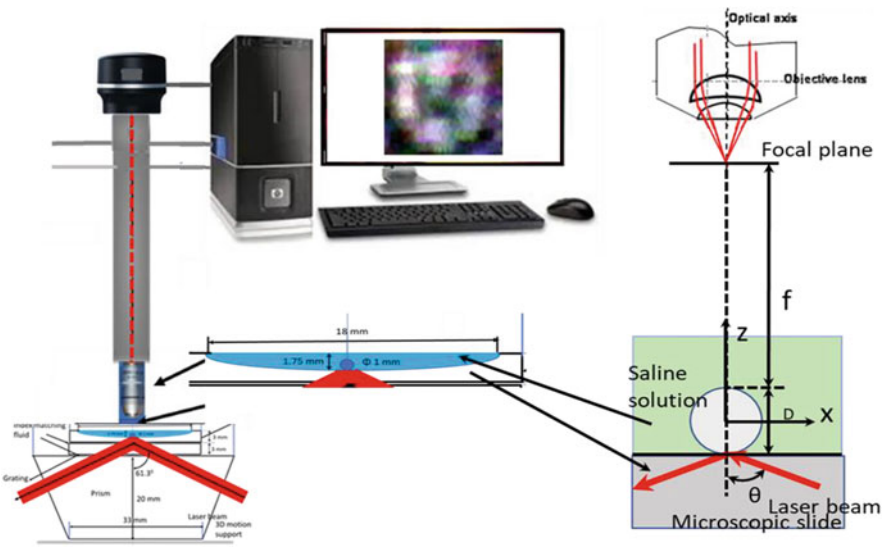

Fig. 1.8 Setup for the detection of dimensions of nano-objects utilizing the whispering gallery equatorial waves

Following the same principle utilized in our original experimental observation of nano-objects, the relay ball lens projects the observed objects into its focal plane. The microscope focus the image on the camera sensor. The digital microscope input goes to a desktop computer that contains all the required software for acquisition of images and data processing. The observed images are displayed in the desktop computer screen.

1.3.2 Role of the Carrier Gratings in the Formation of Images

The spatial resolution of an image depends on the optical resolution of the image-forming lens system and on the resolution capabilities of the utilized sensor. The optical resolution of diffraction-limited optical system is given by the Abbe constrain. It depends on the wavelength of the illuminating light and on the numerical aperture of the lens system. For practical purposes depending on the wavelength of the illuminating beam that is assumed, the limit resolution is either 220 nm or 250 nm. Applying the Nyquist condition for the spatial resolution of 220 nm means that the sampling distance of the sensor must be 110 nm or less to capture the features produced by the lens system. If one has more pixels than is required by the Nyquist criterion, the image will be oversampled, and no additional information on the observed object is gained, but the accuracy can be improved by getting redundant information.

The proposed super-resolution method increases the optical spatial resolution by making available spatial image formation frequencies not attainable with classical illumination procedures. The utilized spatial frequencies to form images can be thought in terms of a classical method utilized in the moiré method, the introduction of carrier fringes to increase the sampling frequency of an image [17]. In this application the sampling tool are carrier gratings introduced in the optical system, Fig. 1.9. It is also essential to define the concept of spatial resolution utilized in this work. Since we are measuring geometrical parameters, the concept of spatial resolution is the measurable distance between points of interest, a concept that is applied in the transmission electronic microscopy [18].

Figure 1.10a shows the image of a 6 μm polyethylene sphere that was part of the optical system that produced the observed images. Figure 1.10a shows the region of the image where the measurement was performed. Figure 1.10b shows a higher magnification image that is obtained by filtering orders in the FFT of the region under observation. In the FFT of Fig. 1.10c are present 120 orders.

The carrier gratings observed in Fig. 1.10b are harmonics of the grating present in the optical circuit, the fundamental carrier of the system.

To connect the quantities of interest in the performed measurements utilizing super-resolution, one can utilize the equation of the light intensity of the field. Calling the u(x,y) the projection of the quantity of interest in the x-axis, and for $y = y_c$, a constant, the intensity along the x-axis is,

$$I(x,y) = I_0\left\{1 + \cos\ \frac{2\pi u(x,y_c)}{p}\right\} \tag{1.8}$$

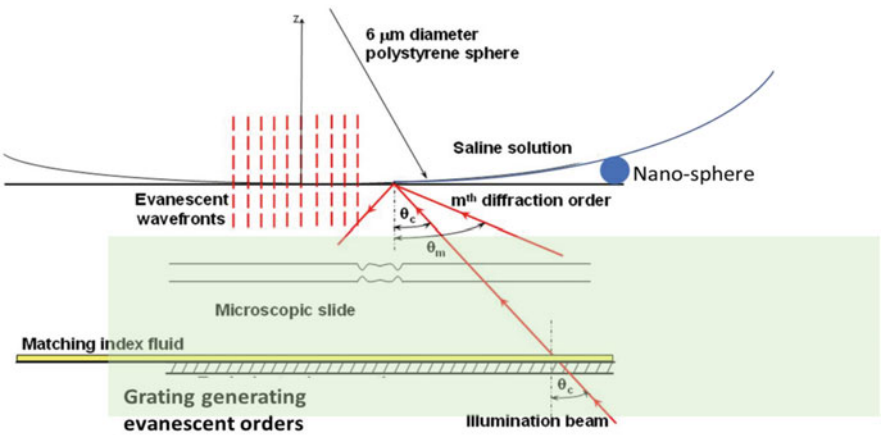

Fig. 1.9 Interface between microscopic slide and nanosphere. Detail of nanosphere position with respect to polystyrene sphere ball lens

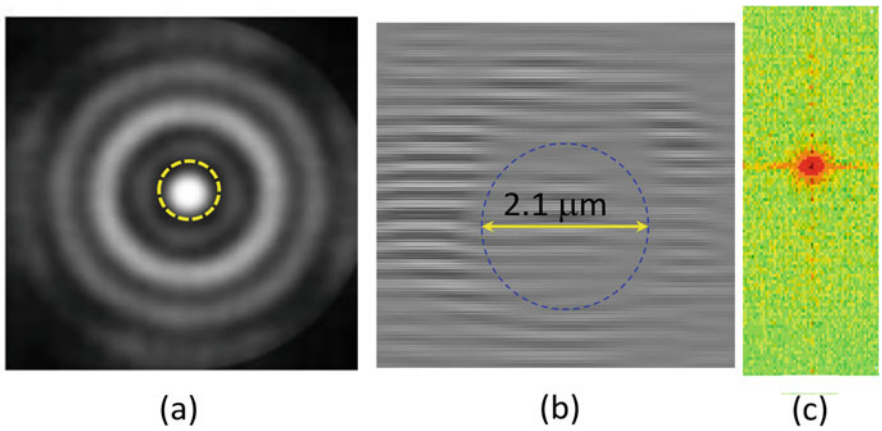

Fig. 1.10 (**a**) Image of the 6 µm spherical ball lens,yellow circle region where the observed nano-objects are located. (**b**)A view of the same region where some of the carrier gratings are shown. (**c**) FFT of the region shown in (a)

where p is the pitch of the selected frequency in the FFT shown in Fig. 1.10c. The value of p changes with the selected diffraction order N, then taking into consideration Eq. (1.8), we obtain a more general expression,

$$I(x,y) = I_0\left\{1 + \cos\ \frac{2\pi u(x,y_c)}{\frac{p_o}{N}}\right\} \tag{1.9}$$

In Eq. (1.9) p_o is the pitch of the grating introduced in the optical circuit. The camera sensor is an essential element in this process since the spatial information must be captured by the sensor and transformed into a digital signal form for further processing. There are two important quantities that define the spatial resolution that can be reached based on a low-cost digital microscope that could be the basis of an inexpensive system to detect the presence of the COVID-19; an example will clarify the process. Commercially available inexpensive digital microscopes can be utilized for this purpose. These microscopes have sensors in the range of the smallest sensors sizes that can be currently manufactured, for example, 1600 × 1200 square pixels of size 1.12 µm. According with these specifications a line-pair is.

$2 \times 1.12 = 2.24$ µm. Utilizing the above sensor and with a magnification of 200 and using a grating of pitch $p_o = 50$ nm, the line-pair dimension is 11 nm. The pixel value is then $11/2 = 5.5$ nm. Selecting the fifth harmonic of the grating, $N = 5$ it is possible to get a pixel size of 1.1 nm. The selection of the pixel size depends on the smallest detail that we want to retrieve in the image. We have shown that it is possible to provide a solution for a particularly important problem that humanity is currently facing, an accurate, inexpensive, and fast process to detect the presence of the COVID-19 virus in a person in real time.

1.3.3 Structure of the COVID-19 Virus

In this section we will describe the geometry of the COVID-19 virus that will enable us to obtain the necessary information via this optical approach [19].

As shown in Fig. 1.11, the COVID-19 19 virus is roughly a spherical shell, and it has a membrane with an average diameter of 85 nm, and an average thickness of 7.8 nm. As such, the ratio of the thickness to radius sphere $t_{th}/r_{sp} = 7.8/42.5 = 0.1835$ is that of a thin shell; inside the membrane is the genetic material of the virus. Attached to the membrane there are several proteins and major spikes of glycoprotein (S). The size of the spikes protruding out of the membrane is 14 nm; the ratio of the length of the protrusion to the radius is $l_{spi}/r_{sp} = 14/42.5 = 0.33$.

What is important to point out is that this ratio is a key characteristic of COVID-19; other corona viruses have different ratios.

In Fig. 1.12b the average ratio between spike size and radius of the virus is 0.34, against the previously mentioned value of 0.33 obtained from a more comprehensive methodology, a 3% difference, value that is within the range of experimental verifications. The transmission electron microscope image clearly shows the virus structure. It is possible to see that sizes and shapes vary in this picture. The virus size is highly variable with average diameter of 85 nm; it can be a minimum of 50 nm and

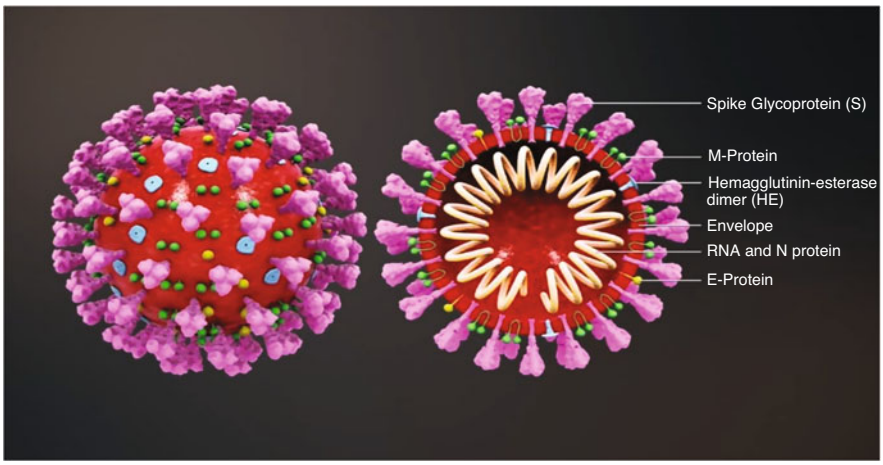

Fig. 1.11 COVID-19 structure

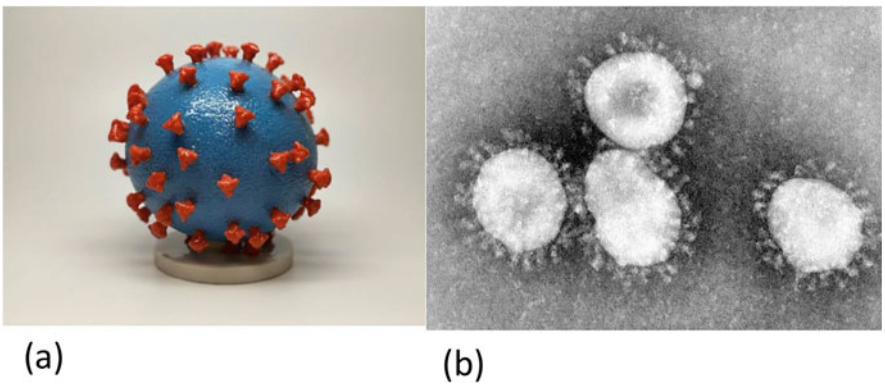

Fig. 1.12 (**a**) 3D reconstruction of the COVID-19 virus showing the spikes; (**b**) Transmission electron microscope image of COVID-19

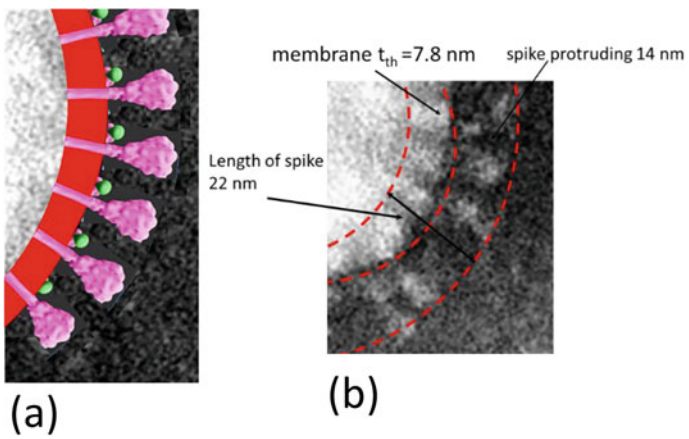

Fig. 1.13 (**a**) An enlarged image taken from Fig. 1.12b showing the membrane and the spikes approximately in scale. (**b**) Actual electron microscope image

can reach 120 nm. The envelope membrane in the transmission electron images appears as a dark region. This characteristic indicates that the membrane produces a minimum intensity in the electron microscope image.

Figure 1.13a shows the reconstruction of a region of the periphery of the COVID-19 virus. Figure 1.13b shows the corresponding image of the region as seen in the electron microscope; it is possible to see that the spatial resolution of the

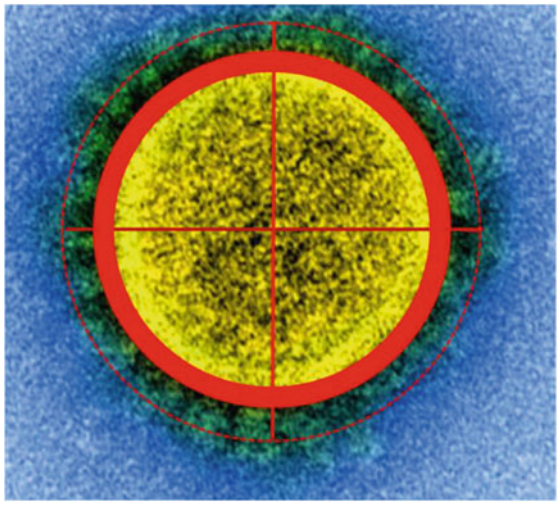

Fig. 1.14 Electron microscopic image of covid-19. Main dimensions; t_{th} is the thickness of the shell

Fig. 1.15 A spike on the COVID-19 virus

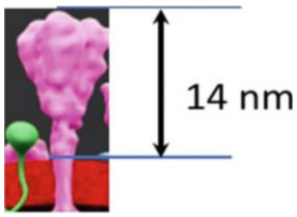

electron microscope is not good enough to define the shape of the spikes shown in Fig. 1.13a. The structure of the COVID-19 is a thin shell with prominent spikes. Figure 1.14 summarizes the main dimensions.

Figure 1.14 shows the geometry of the COVID-19 virus and the principal dimensions**.** An alternative mode to view the virus is to use the whispering gallery mode (WGM) of the spherical resonators described in Sect. 1.3. This methodology applies also to hollow whispering gallery resonators, optical microcavity resonators where light can travel in modes that are supported within the thin wall of the hollow structure. From observations made with dynamic electron microscopy it is possible to conclude that the connection of the spikes to the shell is equivalent to a hinge, since the spikes are in continuous oscillation motion independent of the position of the membrane. In a model of the structure of the COVID-19 virus, the material inside the protective shell can be assimilated to a fluid.

1.4 Model to Develop Techniques of Detection of the Covid-19 Virus

Figure 1.14 provides a starting point to develop a process for the detection of the virus. The cover membrane can be represented as a thin shell, a hollow spherical resonator. The shell interior can be assumed to be fluid. The spherical resonator is in a liquid medium, a saline solution that is added to saliva samples, Fig. 1.9. There are additional components, the spikes shown in Fig. 1.14, that are connected to the shell. The spikes proteins are different from the membrane proteins, as is shown in Fig. 1.15.The emission of light that is the basis of the super-resolution is connected to the vibration of the atoms producing an acoustic wave that results in the conversion of mechanical energy into electro-magnetic energy of the emitted light.

Figure 1.16a shows the standing wave of the WGM along a nanosphere diameter; Fig. 1.16b shows the image in levels of gray of the standing equatorial wave of a nanosphere of 150 nm diameter; Fig. 1.16c shows average intensity and diameter of the nanosphere. Figure 1.16d shows a color image of the same sphere.

The nanosphere is made of polystyrene that has a resonance peak at the wavelength $\lambda = 386$ nm. The wavelength of the violet color emitted light by the nanosphere is $\lambda = 386$ nm, which corresponds to UV radiation. Assuming that simulation shown in Fig. 1.18 produces patterns similar to the patterns of Fig. 1.16, a possible process of detection of the virus based on geometric measurements can be developed.

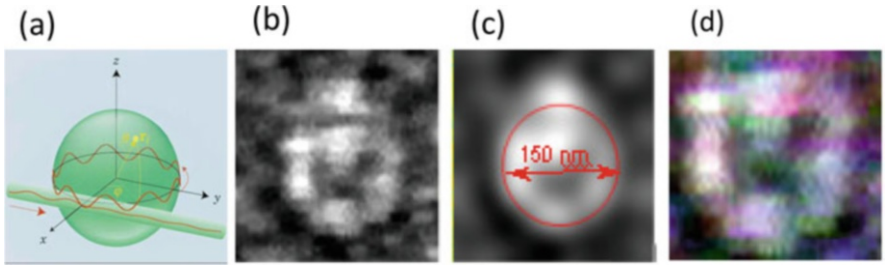

Fig. 1.16 (**a**) Whispering gallery form of oscillation of a nanosphere showing the equatorial stationary wave; (**b**) recorded pattern in levels of gray; (**c**) average intensity and diameter of the nanosphere; (**d**) color image of the same sphere

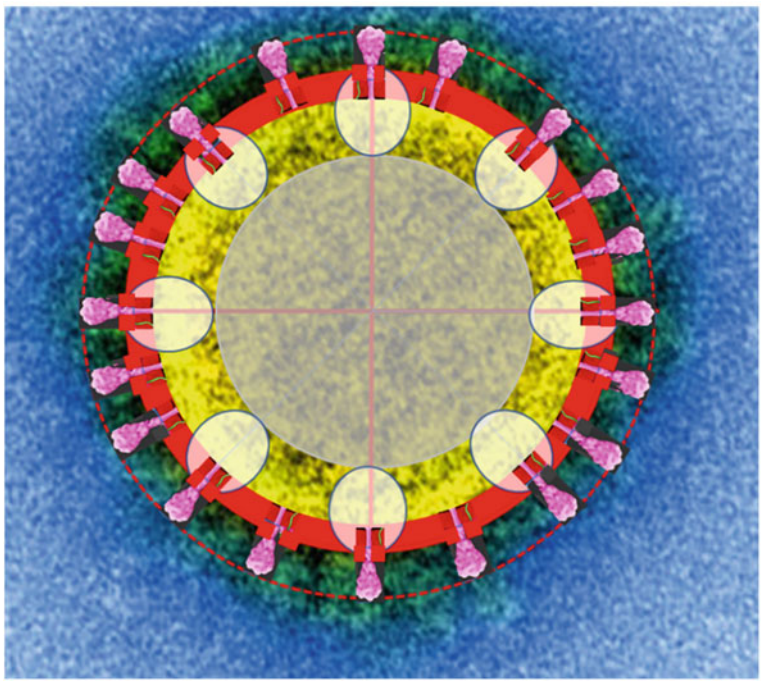

Fig. 1.17 Model of COVID-19 simulating the whispering gallery generated emission for $\lambda = 222$ nm, one of the possible emissions of the protective membrane, red area in the picture

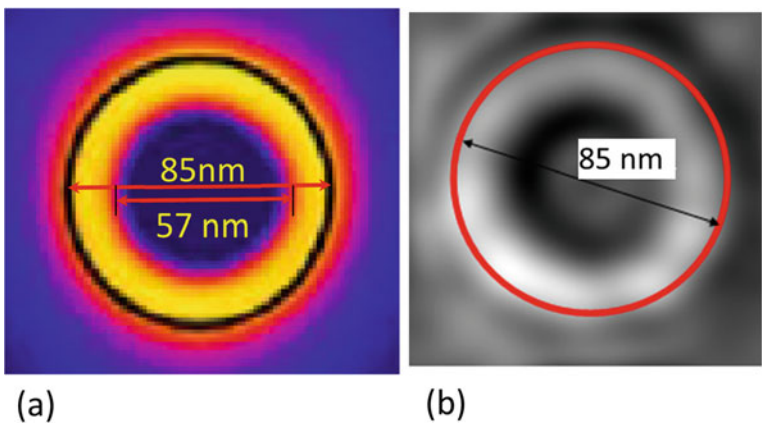

Fig. 1.18 Assumed WGM averaged intensities of nanospheres for a diameter of 85 nm. (**a**) Averages obtained from a numerical mode; (**b**) average from an actual pattern

Figure 1.17 shows a simulation of the of the WGM intensities corresponding to the COVID-19 virus, assuming the average diameter of 85 nm. The bright ellipsoidal elements represent the maximum intensities corresponding to the equatorial wave of the WGM; the maximum axis of the ellipsoid has been selected according to the previously acquired information in the whispering galley patterns of nanospheres shown in Fig. 1.16. From theoretical derivations and experimental evidence, the WGM mode of vibration of a hollow shell is like that of a corresponding sphere. In the simulation shown in Fig. 1.17 in addition of the shell, we have the spikes of the virus. We need to be considered what is the effect of the spikes in the WGM mode of vibration of the nano-shell. Experimental evidence from temporal electron microscopy tells us that the spikes are in continuous oscillation motions that are independent from the shell position. This fact indicates that the connection between shell and spikes can be assimilated to a hinge that allows the oscillation motion of the spikes. Then is highly likely that the WGM mode of vibration is not substantially affected by the spikes. Figure 1.18 shows the average light intensities corresponding to the model of WGM assumed in Fig. 1.17 and accepting that the perturbation caused by the spikes is negligible. Human saliva contains many microscopic components, possibly also including other corona viruses. Consequently, a detection method must have a reliable way to identify the COVID-19 virus and separate it from other corona viruses that may be present in the saliva samples. To detect the COVID-19 one can use dimensional parameters that characterize the COVID-19 specifically and that are different from the dimensional parameters of other corona viruses present in the saliva. This methodology can be applied to high-resolution images similar to the images shown in Fig. 1.16. Different magnifications could be required in the studies connected to COVID-19, if for example it may be necessary to make quantitative evaluations of the viral charge in a saliva sample.

There is an alternative way to detect the presence of the virus that may be applied at different magnification scales. The wavelength of the light emitted by the virus is dependent on the molecular structure of the virus shell. Lasers of diverse optical frequencies may be required to identify the type of proteins of COVID-19 protecting shell that can excite the whispering gallery mode of vibration. Consequently, this fact can produce a signature of the COVID-19 virus creating a reliable identification separating COVID-19 from other corona viruses (Fig. 1.19).

In the periphery of the virus as shown for example in Fig. 1.12 we have the spikes. It is highly likely that due to their motion, the spikes will produce fuzzy images as shown in the electron microscope images. Hence, we will have an additional ring in the image of the virus. This fact is illustrated in Fig. 1.10 where to the pattern of the shell is added a yellow ring corresponding to the presence of the spikes.

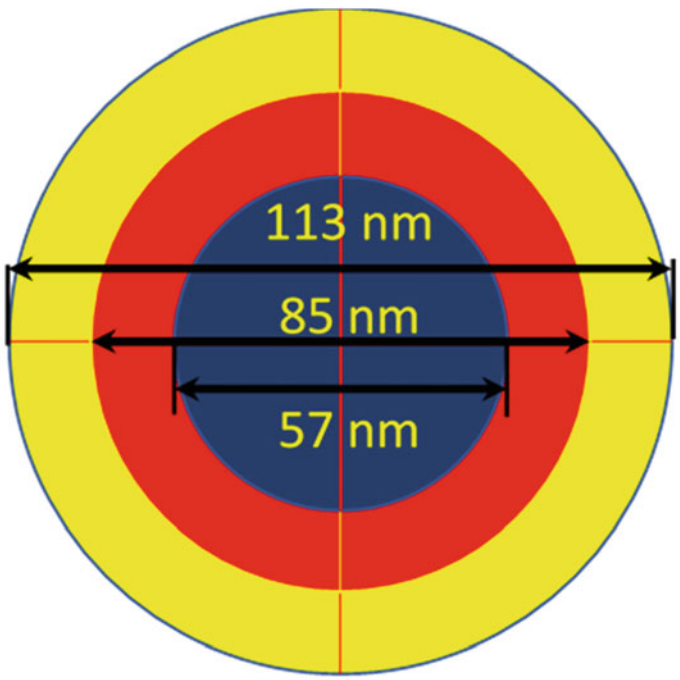

Fig. 1.19 To the parameters of Fig. 1.18, another parameter is added, the total diameter adding to the diameter of the shell the protruding length of the spikes, yellow ring

1.5 Summary and Conclusions

In the literature of developments associated with the COVID-19 pandemic, imaging technologies have a particularly important role in the process of understanding the virus behavior and the developments associated with the mitigation of the virus effects in humans. There is an extraordinary array of available tools for researchers of different aspects of the pandemic. The proposed method can have a dual role, a tool for researchers with the advantage that can be applied in environmental conditions that are close to those that ordinarily surround the virus. At the same time, the proposed method can reach extremely high spatial resolutions without interfering with the virus structure as it occurs with the electron microscope. In addition, the proposed method can be used as a diagnosis tool. Most importantly this methodology can be used to assess the severity of the disease by measuring the viral charge present in the saliva. The goal in this case is to develop as it has previously anticipated, a low-cost setup with extremely high accuracy and introducing the following software features:

1. Automatic focusing.
2. Control programs for the operation of the microscope.
3. Artificial intelligence programs to recognize requested features, and to evaluate number of these features in the analyzed volume.

The outputs should be automatic and independent of the operators' decisions.

References

1. Sciammarella, C.A., Lamberti, L., Sciammarella, F.M.: Experiment Mech. **49**, 747–773
2. Sciammarella, C.A., Lamberti, L., Sciammarella, F.M.: Digital holography to recover 3-D particle information, SEM2005. In: Proceedings of conference on Experimental Mechanics, Portland, USA (2005)
3. Sciammarella, C.A., Lamberti, L.. Optical detection of information at the sub-wavelength level. In: Proceedings of the NANOMEC06 symposium on materials science and materials mechanics at the nanoscale. Modeling, Experimental Mechanics & Applications, November 2006, Bari, Italy
4. Sciammarella, C.A., Lamberti, L.: Observation of fundamental variables of optical techniques in the nanometric range. In: Gdoutos, E.E. (ed.) Experimental Analysis of Nano and Engineering Materials and Structures. Springer, Dordrecht (2007)
5. Sciammarella, C.A., Lamberti, L., Sciammarella, F.M.: Light generation at the nano scale, key to interferometry at the nanoscale. Experiment Appl Mech. **6**, 103–115 (2010)
6. Sciammarella, C.A.: Experimental mechanics at the nanometric level. Strain. **44**(1), 3–19 (2008)
7. Sciammarella, C.A., Lamberti, L., Sciammarella, F.M.: Optical holography reconstruction of nano-objects. In: Rosen, J. (ed.) Holography, Research and Technologies, pp. 191–216. InTech, Rijeka (2011)
8. Brillouin, L.: Les électrons dans les métaux et le classement des ondes de de Broglie correspondantes. C. R. Hebd. Seances Acad. Sci. **191**, 292–294 (1930)
9. Brillouin, L.: Course De Physique Théoretique. Mason et Cie, Paris (1938)
10. Burch, J.W., Gates, C., Hall, R.G.N., Tanner, L.H.: Holography with a scatter-plate as a beam splitter and a pulsed ruby laser as light source. Nature. **212**, 1347–1348 (1966)
11. Spencer, R.C., Anthony, S.A.: Real time holographic moiré patterns for flow visualization. Appl. Opt. **7**, 561 (1968)
12. Pack, A.: Current topics in nano-optics. PhD Dissertation. Chemnitz Technical University, Chemnitz (2001)
13. Bouchal, Z.: Non diffracting optical beams: physical properties, experiments, and applications. *Czechoslovak J Phys*. **53**, 537–578 (2003)
14. Hernandez-Aranda, M.: Guizar-Sicairos and M.A. Bandres. "Propagation of generalized vector Helmholtz-Gauss beams through paraxial optical systems". Opt. Express. **14**, 8974–8988 (2006)
15. Durnin, J., Miceley, J.J., Eberli, J.H.: Diffraction free beams. Phys. Rev. Lett. **58**, 1499–1501 (1987)
16. Gutiérrez-Vega, J.C., Iturbe-Castillo, M.D., Ramirez, G.A., Tepichin, E., Rodriguez-Dagnino, R.M., Chávez-Cerda, S., New, G.H.C.: Experimental demonstration of optical Mathieu beams. Opt. Commun. **195**, 35–40 (2001)
17. Sciammarella, C.A., Sciammarella, F.M.: Experimental Mechanics of Solids. Wiley, Chichester (2012)
18. Williams, D.R., Carter, B.: Transmission Electron Microscopy, a Textbook for Materials Sciences, 2nd edn. Springer, New York (2009)
19. Images of the covid-19 shown in this paper are taken from the Image Library of CCD Newsroom where the original references are provided